Original Article

Microfluidic platform for coupled studies of freezing behavior and final effloresced particle morphology in Snomax® containing aqueous droplets.

Margaret L. House[a], Cari S. Dutcher[a],[b]

[a] Chemical Engineering, University of Minnesota Twin Cities, Minneapolis , MN, USA; [b] Mechanical Engineering, University of Minnesota Twin Cities, Minneapolis , MN, USA

CONTACT

Cari S. Dutcher, cdutcher@umn.edu, Mechanical Engineering, University of Minnesota Twin Cities, 111 Church St., Minneapolis, MN, 55455, USA.

ABSTRACT

Aerosol physicochemical mixing state, defined as the chemical, phase, and internal structure of a population of aerosols, is complex and under-characterized regarding its role in the atmosphere. The compositional and microphysical properties of the aerosol particle strongly impact its atmospheric processes, including water uptake and ice nucleation (IN) activities. However, the relationship between IN activity and particle microphysics remains underdeveloped, as the aerosol particle IN activity, composition, morphology and size are highly intercorrelated. In this article, we demonstrate the efficacy of a microfluidic static well trap device for testing both IN activity and effloresced residual particle morphology in the same droplet. We link cationic composition with both IN activity and residual particle morphology in droplets containing sodium chloride, calcium chloride, and the biological ice nucleating particle (INP) Snomax. Finally, we show a decoupling between IN activity and residual particle morphology within the same droplet for the chemical systems studied here.

1. Introduction

While aerosols have been studied since the 19th century (Hidy 2019), many of their impacts on human health and climate are still under-characterized on a mechanistic level, in part due to the compositional complexity of the individual particles. On short spatial and temporal scales, studying the link between chemical composition and the generation (Lindsley et al. 2012), transport (Ahlawat et al. 2022), and deposition efficiency (Legh-Land et al. 2021) of respiratory aerosols remains a key challenge. On larger spatial and temporal scales, systems of aerosols in the atmosphere, known as atmospheric aerosols, influence global climate and the energy balance of the earth (Szopa et al. 2021). Atmospheric aerosol particles are compositionally complex, and can be comprised of water, organics, soot, dust, salt, and biological components (Hinds 1999). For example, inorganic salts can be introduced over the ocean, where breaking waves generate sea spray aerosols (SSA) high in sodium chloride, calcium chloride, and other salts. Biological matter in aerosols such as pollen (Steiner et al. 2015), bacteria and fungi (Beall et al. 2021), and viruses (Reche et al. 2018) can vary seasonally and with geographic location (Burrows et al. 2009). Once suspended in the atmosphere, the particles composition and microphysical properties can be further altered with aging and changes of ambient conditions.

Aerosol mixing state, defined as the distribution of physical and chemical properties of particles within a suspended aerosol population, is an important predictor of atmospheric interaction parameters in aerosol particles. This broad definition of mixing state can be split into two categories: the more well studied chemical mixing state, defined as the distribution of chemical species across individual particles within an aerosol population, and the less well understood physicochemical mixing state (Riemer et al. 2019). Defined by Ault & Axson, physicochemical mixing state refers to the phase and internal structure of the particles in an aerosol population, providing both chemical and spatial information (Ault and Axson 2017). Chemical and physicochemical mixing states are impacted by the initial chemical composition of the aerosol droplet, as well as by atmospheric aging processes in which the droplet undergoes chemical reactions, phase changes, and evaporation. Both chemical and physicochemical mixing states change the optical properties of aerosol particles directly (Yao et al. 2022). They impact the ability of particles to act as cloud condensation nuclei (CCN), commonly referred to as CCN activity (Vu et al. 2019), (Stevens and Dastoor 2019). Chemical mixing state impacts the ice nucleating (IN) activity of individual particles, where the particles which can nucleate ice within clouds are referred to as ice nucleating particles (INP). Differences in the amount and type of INP can change the overall albedo of clouds by causing portions of the cloud to freeze, leading to greater optical extinction through the cloud (Vergara-Temprado et al. 2018).

Partially frozen clouds, commonly referred to as mixed-phased clouds, are known to be common over the Arctic and the Southern Ocean, greatly influencing the radiative budget in these areas (Korolev et al. 2017). Global climate models are still not fully able to represent the contribution of mixed-phase clouds to overall climate (Mccoy et al. 2016). INP enable the heterogeneous freezing that can lead to mixed phase clouds, but uncertainties remain in their contribution to global climate (Bellouin et al. 2020) partially because different aerosol compositions create a complex set of ice nucleation pathways that are not fully characterized (Knopf, Alpert and Wang 2018). Continuing efforts to establish connections between ice nucleation activity and the aerosol particles chemical and physical properties are needed, as it is important for the predictive power of global climate models (Riemer et al. 2019).

In the puzzle of physical and chemical properties that contribute to the physicochemical mixing state of an aerosol population, particle morphology is one important piece. Particle morphology in the atmosphere can be a spectrum of shapes and phases, with some particles being nearly spherical, and others having highly disordered fractal shapes or multiple phases. As aqueous droplets evaporate, they form dry residual particles, whose shapes and sizes may be dependent on composition (Hasenkopf et al. 2016), ion type (Ott and Freedman 2021), drying rate (Altaf and Freedman 2017) , aging (Kaluarachchi et al. 2022), Peclet number (Wang et al. 2021), and confinement (Kohler, Pierre-Louis and Dysthe 2022). Residual particles of different morphologies behave differently in the atmosphere, and the link between particle morphology and IN activity is still currently being investigated. IN activity has been shown to be a function of composition (Baustian et al. 2012; Demott et al. 2003; Peterson and Tyler 2003), particle size (Reicher et al. 2019), and surface chemistry (Zhang et al. 2020). However, the relationship between IN activity and particle morphology is less clear. In biomass burning aerosol, particle source can change the morphology and IN activity of the resulting aerosol (Mahrt et al. 2023), and atmospheric aging removes organic surface coatings on biomass burning aerosol enhancing their IN activity (Jahl et al. 2021). Some studies in inorganic (Gao et al. 2022) and urban (Hasenkopf et al. 2016) aerosols have suggested IN ability is linked to particle morphology. Advanced methods are needed to aid in relating IN activity and residual particle morphology for individual particles of a given size and composition.

Single particle measurement techniques are important tools for studying physicochemical properties of particles of varying composition, shape, and size. Krieger, Marcolli, and Reid reviewed common methods of isolating single aerosol or model-aerosol particles for chemical analysis, and subsequent measurement of important aerosol properties like hygroscopicity and particle morphology (Krieger, Marcolli and Reid 2012). The authors identify ways in which single particles are isolated, such as with electrodynamic balances (EDBs) and optical tweezers. Atmospheric parameters like hygroscopicity, hygroscopic growth, morphology, and phase separation can then be observed by measuring mass changes and observing phase domains with optical microscopy. For the study of INP, immersion freezing and continuous flow diffusion chambers (CFDC) have been used to explore the IN activity of multicomponent aerosol droplets from marine (Demott et al. 2016) and overland (Suski et al. 2018) environments. Immersion freezing can be combined with Raman spectroscopy for chemical analysis (Mael, Busse and Grassian 2019).

Microfluidic methods have emerged comparatively recently in the field of atmospheric aerosol science, as a complementary approach to single droplet work. A review into current microfluidic methods for studying droplets, including those of atmospheric relevance, has been given by Roy, Liu, and Dutcher in Annual Reviews of Physical Chemistry, 2021. Briefly, fluid flows can be used to determine the changing optical, thermodynamic, and rheological properties of a droplet through time, leading to information about events like freezing and phase separation. Examples of flow-through devices for ice nucleation include the MINCZ (Isenrich et al. 2022) and the flow-through devices used by the Murray group (Tarn et al. 2021) and the Dutcher group (Roy, House and Dutcher 2021). Alternatively, trapped droplets can be observed with an optical microscope under decreasing temperature and/or relative humidity (RH), and information about the number and type of phase transitions, as well as effloresced particle morphology, can be linked to droplet composition. Examples of static devices for ice nucleation include the WISDOM (Reicher, Segev and Rudich 2018) and the static well arrays used by the Sullivan group (Brubaker et al. 2020) and the Dutcher group (Nandy et al. 2019). Microfluidic techniques can be combined with Raman spectroscopy for chemical analysis, and microfluidic devices can be temperature controlled to study low temperature phase changes and freezing. (Roy et al. 2021; Roy et al. 2020). Because of the ability to combine temperature and RH control in a single microfluidic device, microfluidic platforms offer unique opportunities for elucidating the relationship between IN activity and residual particle morphology.

In their 2021 article, Roy et al. utilized a static well trap microfluidic device to collect a freezing assay of ~150 nanoliter-volume seawater and sea surface microlayer (SSML) samples (Roy et al. 2021). These same droplets were then dried, and information about the size and shape of the residual particles was obtained using optical microscopy. Information about particle composition was further explored using Raman spectroscopy, as well as heat and chemical treatments. The authors concluded that residual particle morphology and IN activity in the same aerosol particle were potentially related, with particles resulting in aggregate or amorphous appearing to have a slightly warmer IN spectrum than those with a crystalline morphology. The study was performed with seawater-based samples, with a range of ion types present.

In this article, we seek to explore this possible relationship between particle morphology and IN activity using the Roy et al. microfluidic method for coupled freezing and efflorescence experiments on the same droplets, but now utilizing a model aqueous aerosol system comprised of known amounts and ratios of inorganic salt and organic material. In section 2, we discuss the method adapted from Roy et al. for freezing and residual particle morphology testing in a microfluidic well device and outline the compositional ratios of salts and organics used in our model system. In section 3, we show the efficacy of our device in capturing complex biological IN behavior in Snomax bacteria and demonstrate the important role of the Ca^{2+} cation in both freezing behavior and residual particle morphology. In section 4, we discuss the interaction between the Ca^{2+} cation and the biological particles in our model system and explain how our results suggest decoupling of IN activity and residual particle morphology in the same droplet.

2. Methods

To fabricate the microfluidic devices used in all freezing and drying experiments, a "master mold" was first created using standard photolithography techniques, as detailed in previous works (Narayanan 2011), (Stan et al. 2009), (Roy et al. 2020), (Narayan et al. 2020). The mold is used to pattern polydimethylsiloxane (PDMS) with the device features. The PDMS device is fixed to a PDMS-coated glass slide as a backing. Details on photolithography techniques and device fabrication are provided in the online Supplemental Information. The device design is based on similar static well trap devices, such as those in (Nandy et al. 2019), (Roy, Liu and Dutcher 2021). The large well array design for IN studies is based on a similar design by Brubaker et al (Brubaker et al. 2020) as shown in Figure 2b, with modifications to the channel dimensions and the number of inlet and outlet ports to make loading droplets of the desired working fluids more reliable and efficient, as shown in Figure 1a. As shown in Figure 1b, the well diameter is 450 μm; it should be noted that volume and confinement can play an important role in both freezing (Alba-Simionesco et al. 2006; Ginot et al. 2020) and efflorescence (Li et al. 2018). Volume analysis of droplets from the optical microscopy is described in Section 3.1. To load droplets into the microfluidic device, all channels are first flushed with filtered silicone oil (Whatman PTFE Filter, 0.1 um). Then, a syringe with a 1.2mm needle is used to fill all channels and wells with the sample to be tested. Finally, filtered silicone oil is again injected into each channel so that the channels are cleared of excess aqueous sample while droplets of sample remain trapped in each well. The array stores 150 droplets total.

Figure 1

All freezing experiments take place on a temperature-controlled cold stage (LTS 420 with LNP96 cooling pump, Linkam Scientific). A mirror is placed between the cold stage and the device to reflect the image of the device to the reflected light microscope (SZX10, Olympus). Thermal grease (Ceramique 2, Arctic Silver) is used to ensure good thermal contact between the mirror and cold plate. Several drops of silicone oil are placed between the loaded device and the mirror to enhance thermal contact. Thermocouples (K Type Mini-Connector Thermocouple, HUATO Environment Monitoring System and Equipment) are slotted into each thermocouple channel, shown in Figure 2a after the tips are coated in thermal grease. The device temperature, defined as the average of the four thermocouple temperatures, is calibrated using the known melting points of hydrocarbons, as detailed in the online Supplemental Information. The typical standard deviation of the temperature across the four thermocouples was approximately 1°C. Analysis of the temperature error is provided in the online Supplemental Information. Pure water and water–salt samples, after correcting for freezing point depression, freeze below -20 °C, with an average pure water freezing temperature (T50) of -30°C. While above the homogeneous freezing temperature due to possible environmental contaminants in the PDMS or impurities in the water (Polen et al. 2018), the background freezing is well below the IN spectra for the aqueous Snomax samples studied here. Finally, a custom-made acrylic box is placed over the device and cold stage, and dry nitrogen gas at a rate of about 5 SLPM is used to purge the atmosphere in the box so that condensation on the device and cold stage surfaces can be avoided during experiments. Condensation remains a challenge in the humid summer months, limiting the number of tests that can be performed in the summer.

Figure 2

The temperature of the cold stage is dropped to -4°C and held there for five minutes to ensure that the thermocouples have been inserted properly by checking the measured temperature. Then, the droplets are cooled at a rate of 1°C per minute until all droplets are frozen. A video is taken of the freezing droplets with a 1200x1600 px monochromatic camera (acA1600-60gm, Basler) attached to the microscope. After all droplets are frozen, the device is warmed to room temperature at a rate of 10°C/minute, and all droplets melt. The thawed device is placed in a chamber at <5% RH. The relative humidity gradient in the PDMS between the droplets and the dry air causes water molecules to pervaporate from the droplets through the device into the ambient air. When all the water evaporates from the droplet, salts, bacterial matter, and organic matter are left behind and form crystal structures that differ in shape and optical properties (Nandy and Dutcher 2018). The residual crystal or particle left in each well is photographed with a camera (Basler) and the pictures are sorted manually to classify the particle type.

Aqueous samples were prepared using HPLC water (Fisher Scientific). The HPLC water was filtered with a 0.02 μm PTFE Whatman filter before mixing to minimize impurities from the background water and salt water samples. Background freezing information can be found in the SI. Snomax (Snomax International, Englewood, CO, USA) was stored in freezer at -5°C until use to prevent aging. NaCl (Fisher Scientific) and $CaCl_2$ (dihydrous, Millipore Sigma) were used to study salts with two different cations. Table 1 shows the concentrations of salts, and Snomax in each mixture.

Table 1

The 5.25:1 NaCl:$CaCl_2$ molar ratio was chosen because of its relevance to enrichment in SSA, where Ca^{2+} is seen to be enriched from seawater, as further detailed in Section 4.2. To test the effects of physiochemical degradation on Snomax bacteria, samples were heated in a water bath. Samples labeled "HT 7min" were heated to 80°C for 7 minutes. Samples labeled "HT 10min" were heated to 80°C for 10 minutes. Samples labeled "denatured" were heated to 100°C for 20 minutes.

3. Results

3.1 Comparing to Literature Results for Device Validation

The first step in carrying out the large well array crystallization experiments was to verify that the device design performed comparably to other similar devices and methods for measuring the freezing behavior of warm ice nucleators like Snomax. To make this comparison, the ice nucleating active site density, or the number of ice nucleating active sites per milligram of Snomax bacteria, abbreviated as η_m, was calculated. To calculate η_m, the fraction of droplets frozen in the device, called the frozen fraction, is first calculated as a function of temperature, as shown in Equation 1.

$$f(T) = \frac{N_f}{N} \qquad (1)$$

Where N_f is the number of frozen droplets at a given temperature T, and N is the total number of droplets visible in the viewing window. Temperature from the four thermocouples is averaged across the device. Once frozen fraction as a function of temperature is calculated, η_m can be modeled as a time-independent function of temperature, as shown in Equation 2 (Vali 1971).

$$n_m(T) = -\frac{\ln(1 - f(T))}{V \times C_m} \tag{2}$$

Where η_m is ice nucleating active site density (INAS/mg), V is droplet volume, and C_m is the concentration of the ice nucleating material in the bulk solution, in this case Snomax. Since droplets in the microfluidic device are pressed into a "pancake" shape, volume is approximated as a cylinder with the semicircular border, as shown in Equation 3 (Vuong and Anna 2012), (Nandy and Dutcher 2018),

$$V = \frac{\pi h^3}{6} + \frac{\pi h}{4}(D_{drop} - h)\left(\frac{\pi h}{2} + D_{drop} - h\right) \tag{3}$$

where h is the channel height and D_{drop} is the diameter of the droplet.

The ice nucleating active site density measured in our device is plotted in Figure 3, along with values from several other works focusing on Snomax IN activity. In theory, η_m should be consistent across temperature for any INP. In practice, Snomax is known to have varying η_m over a wide range of temperatures. This variation can be caused by age of the Snomax (Polen, Lawlis and Sullivan 2016), storage method (Beall et al. 2020), and testing method (Wex et al. 2015).

Figure 3

Our freezing curve and INA density of Snomax bacteria agree with literature values. Snomax has been postulated to contain three classes of ice nucleators; class A nucleates ice above -4.5°C, class B nucleates ice between -4.5°C and -6.5°C, and class C nucleates ice below -6.5°C (Turner, Arellano and Kozloff 1990). It has been theorized in recent work on Snomax that class A and C INP dominate, with few class B INPs (Wex et al. 2015), (Schwidetzky et al. 2020). This explains the plateau region of the curves from around -4.5°C to -6.5°C, which our device captures.

3.2 Freezing Point Depression

The freezing point depression of the saline aqueous mixes, ΔT_f, was calculated using Blagden's Law for ideal dilute solutions, given by Equation 4,

$$\Delta T_f = iK_f m \tag{4}$$

Where i is the van't Hoff factor, or the number of cations per molecule of solute, K_f is the cryoscopic constant of the solvent, and m is the molality of the solution. Using Blagden's Law, the freezing point depression for each mixture is -3.72 °C for the NaCl containing systems, 5.58°C for the $CaCl_2$ containing systems, and 4.02°C for the systems containing a 5.25:1 molar mix of NaCl to $CaCl_2$. The freezing temperatures reported here are adjusted by these values in order to compare across samples. In tests of the saline aqueous mixtures compared to pure water, these constant offset values for freezing point depression accurately matched the freezing curves to within the error bars of our devices.

3.3 Cation Dependency Across Treatments

Figure 4

Frozen fraction versus temperature and cumulative INAS density, K(T), versus temperature are shown for the monovalent NaCl and Snomax mixture, the divalent $CaCl_2$ and Snomax mixture, and the 5.25:1 NaCl:$CaCl_2$ mix in Figure 4. These curves are corrected for freezing point depression. Heat treatments were applied because they had a predictable effect on the ice nucleating proteins in the Snomax bacteria, flattening the beta helix structures into beta sheets (Roy, House and Dutcher 2021) and inactivating the bacteria's ice nucleating capabilities. The effect of this flattening could then be compared across cation differences. In addition, we could observe the effect of gradual Snomax denaturation on final effloresced particle morphology. Even after freezing point depression correction, the mixture of 1M divalent $CaCl_2$ shows a significantly lower freezing activity than the monovalent mixture. The divalent curves are also more "spread" than the monovalent curves, with more warm and more cold freezers. To potentially distinguish slight differences in INAS density more clearly between the fully monovalent mixture and the monovalent – divalent mixture, the derivative form of INAS, k(T), was also calculated for these cases. The results of the derivative calculation are included in the online Supplemental Information. The role of cation enrichment on the IN activity will be discussed in more detail in Section 4.2.

After determining our systems' freezing behavior observed in the device, the next goal of the experiments was to explore the link, if any, between freezing point and crystal morphology. To do this, it was convenient to create five “bins” to sort different final crystal morphologies into. The categories are shown in Figure 5. These categories are not discrete: rather, they represent a spectrum of disordered behavior in the final crystal morphologies observed in the wells. Similar methods of binning morphology into broad categories are used into aerosol science communities, particularly for substrate based single particle methods (Kaluarachchi et al. 2022; Lei et al. 2022; Roy et al. 2021).

Figure 5

Figure 6 shows the percent of each particle type for different mixtures of salt and Snomax, as well as across heat treatments. The NaCl mixtures and the divalent – monovalent salt mixtures form very different final particles, with the majority of purely monovalent salt particles being single or fractal, as expected, and no single or fractal particles present in the monovalent divalent mixture. The ‘coated’ crystal type (shown with crosshatches) also emerges with the introduction of the divalent salt, and is not observed in the purely monovalent case. Without Snomax bacteria present (“No SM”), the final residual particles for pure NaCl are more ordered than when Snomax is present. This is true even when the Snomax bacteria is inactivated. The prevalence of the coated particle type may be highest when the Snomax bacteria is partially denatured. However, taking the ± 4% error bars associated with device-to-device variability, there appears to be no correlation between the level of Snomax denaturation and the final particle morphology distribution observed.

Figure 6

4. Discussion

4.1 Crystal Type versus Freezing Temperature

Figure 7

Overall, there is no dependency observed for the monovalent/divalent mix between final particle type and freezing temperature, as shown in Figure 7. In the fully monovalent mixture, there is a weak dependency on temperature, where single particle wells appear to freeze at a higher temperature on average than the other wells. However, due to low sampling numbers in the “single” category and sometimes the “aggregate/amorphous” category, these differences are not found to be statistically significant. Melting and then subsequently refreezing after efflorescence and deliquescence in the same wells was carried out for the mixture of interest, 1M NaCl:SM. The refreezing behavior is discussed in Section 4.3 and the online Supplemental Information.

4.2 Enrichment of Ca^{2+} and the effects on freezing and particle morphology

Comparing our results to the results of Roy et al 2021 when linking freezing temperature to efflorescence particle morphology for real seawater samples, Roy et al attributed the high level of disorder in the effloresced particles to the presence of high levels of organics, namely sialic acid. Our results show that the presence of biological compounds like Snomax bacteria, even in low concentrations, can also have an affect on final particle morphology. Roy et al may have observed a larger fraction of the coated particle type in their studies- this could be due to the presence of other salts besides NaCl and $CaCl_2$, such as $MgCl_2$.

It is understood that divalent cations are enriched in SSA and SSML (Jayarathne et al. 2016), (Mukherjee, Reinfelder and Gao 2020; Oppo et al. 1999), (Mukherjee, Reinfelder and Gao 2020) and that these divalent cations lead to the enrichment of other, organic components in SSA (Schill et al. 2018). Ca^{2+} has been shown to be enriched in SSA, though the reason behind enrichment is not agreed upon. Suggested mechanisms include Ca^{2+} complexing to carbonate or organics(Salter et al. 2016), biogenic CaCO3 such as calcareous phytoplankton fragments (Hawkins and Russell 2010), (Sievering 2004), and shell fragments (Keene et al. 2007). A recent study by de Vasquez et al on the binding of calcium and magnesium ions shows that calcium preferentially binds as a contact ion with carboxylate (Vazquez De Vasquez et al. 2021). Our estimate for the enrichment of Ca^{2+} in our 5.25:1 molar ration Na:Ca mixture is based on a comprehensive study by Bertram et al. which gives recommendations for the mass fractions of salt used in laboratory mimics of SSA (Bertram et al. 2018). It is important to note that a key limitation of microfluidic methods is that the size distribution of sea spray and other aerosol is not preserved. Since the homogeneous freezing point changes with droplet volume, this could impact our observed freezing results.

1 M $CaCl_2$ had a much lower freezing efficiency than 1 M NaCl when mixed with equal amounts of Snomax bacteria, as well as a broader spread of freezing temperatures. This trend persisted when the Snomax was heat treated. The lower freezing efficiency could be caused by the gelation of the Snomax

bacteria, since Ca^{2+} is known to gel biological components (Richards et al.), (Silva et al. 2003). However, the 5.25:1 mixture showed no statistical difference in freezing behavior from the mixture containing only NaCl. This suggests that sodium chloride dominates freezing behavior, even in SSA enriched in calcium cations. It is only in the phase change of the particles with decreasing relative humidity that a difference in phase between a monovalent only mixture and monovalent-divalent mixture is observed. This is further confirmed by the results of Roy et al 2021, where bulk seawater and SSML did not show differences in freezing behavior but showed differences in final particle morphology.

4.3 Bacterial entrainment and halotolerance

It has been observed that bacteria can be entrapped within fluid inclusions in salt crystals, both laboratory grown (Adamski, Roberts and Goldstein 2006) and naturally occurring in a marine environment, and that the bacteria can survive and mutate to become more halotolerant (Elabed et al. 2019). The survivability of bacteria in high salinity conditions has become an area of great scientific interest as the saline lakes on the planet Mars are studied and modeled (Cesur et al. 2021), (Benison 2019). Many of the visible imperfections in the single and fractal particles in our model mixtures could be fluid inclusions; this could be confirmed by use of Raman spectroscopy (Haixia and Guoxiang 2015).

The Snomax bacteria entrained in the fluid inclusions may be denatured partially or fully because of exposure to high salinity. In a 2020 study, Karimi et al observed that P. syringae strains isolated from Snomax had no IN activity in NaCl solutions above 7% w/w NaCl (Karimi et al. 2020). To explore the halotolerance of Snomax bacteria, fully effloresced Snomax-NaCl particles were rehydrated in a 100% humidity environment. There was no correlation observed between the freezing order in the first test, before drying, and the freezing order in the second test, after drying-deliquescence-partial rehydration with the untreated 1 M NaCl:SM mixture. Further discussion of the details of rehydration tests is provided in the online Supplemental Information.

Finally, it is important to contextualize our results within the larger research space of freezing behavior and efflorescence of confined droplets. It is known that confinement plays a role in freezing, both in experiments and in the atmosphere. Experimentally, it has been shown that fluid-fluid and fluid-wall interactions in a confined environment have pronounced effects on freezing, and that the hydrogen bonding present in water causes water confined in pores to freeze at lower temperatures than the bulk (Alba-Simionesco et al. 2006). This pore freezing is theorized to occur in the atmosphere in aggregate dusts and other porous particles (Marcolli 2014), and is impacted by solute (Ginot et al. 2020). However, this behavior is often observed in pores on the nanometer scale, which are much smaller than our microfluidic wells. Confinement is also known to play a role in crystallization (Kohler, Pierre-Louis and Dysthe 2022), and a wide range of microfluidic techniques have been used to study crystallization rate and final particle morphology under confinement (Meldrum and O'Shaughnessy 2020). While it may be impossible to rule out confinement effects in our observations in the current study, it should be noted that all final particles compared to each other were under the same degree of confinement.

5. Conclusion

Model marine-origin aerosols were studied using a 150-well microfluidic device in order to establish what link, if any, exists between composition, IN activity, and effloresced particle morphology. Droplets were loaded into the static 450 μm wells, frozen, thawed, and then dried at room temperature until efflorescence of the particle occurred. Particle composition ranged from 1 M NaCl, the totally monovalent case, to 1 M $CaCl_2$, the totally divalent case, with an intervening composition of 5.25:1 NaCl:$CaCl_2$ to represent the most common enrichment of $CaCl_2$ in SSA. The ice nucleating bacteria Snomax was added to represent biogenic INP found in seawater. $CaCl_2$ decreased the IN activity of the droplets, possibly due to gelation of the Snomax bacteria forming aggregates with fewer ice nucleating active sites. The addition of Snomax bacteria affected the final particle morphology distribution of effloresced particles, and stepwise heat treatment of the Snomax, which denatured the ina-Z protein responsible for ice nucleation, did not affect the final particle morphology distribution. In addition to organic aerosol and biological INP, the method reported in this paper is useful for studying the IN activity of inorganic particles such as dust, providing a platform for future studies on the effect of RH cycling on IN activity on a single droplet level.

When comparing the average freezing temperature of final particle categories for NaCl in Section 4.1, freezing temperature and final particle morphology appear to be decoupled. This suggests that final particle morphology is more likely rate dependent, volume dependent, and dependent upon the degree of confinement of the initial droplet. This theory is further confirmed by the fact that denaturing the Snomax with heat has no measurable effect on the final effloresced particle morphology distribution as a whole. This behavior warrants further study with varying drying rates, which can be completed in a relative humidity control chamber, but which is outside of the scope of this paper. Snomax bacteria appeared to be denatured by the highly saline conditions undergone during the drying process. This has wider implications in the atmosphere in general, suggesting that halotolerant biogenic INP may remain more IN active through RH changes than their non-halotolerant counterparts, and that particle phase change due to RH may permanently affect IN activity by denaturing key proteins in biological INP.

Acknowledgments

The authors thank collaborators from NSF CAICE, especially Kathryn Moore, Paul DeMott, and Thomas Hill for insight on ice nucleation experiments, Dutcher group alumnus Priyatanu Roy for manuscript feedback, and Dutcher group member Iaroslav Makhnenko for device fabrication assistance.

Funding

This work was supported by NSF through the NSF Center for Aerosol Impacts on Chemistry of the Environment (CAICE), an NSF Funded Center for Chemical Innovation (CHE-1801971). Portions of this work were conducted in the Minnesota Nano Center, which is supported by the National Science Foundation through the National Nanotechnology Coordinated Infrastructure (NNCI) under Award Number ECCS-2025124. Any opinions, findings, and conclusions or recommendations expressed in this material are those of the authors and do not necessarily reflect the views of the National Science Foundation.

ORCID

Margaret House: 0009-0002-7191-3985

Cari Dutcher: 0000-0003-4325-9197

References

Adamski, J. C., J. A. Roberts, R. H. Goldstein. 2006. Entrapment of bacteria in fluid inclusions in laboratory-grown halite. *Astrobiology* 6:552-562. doi: 10.1089/ast.2006.6.552.

Ahlawat, A., S. K. Mishra, H. Herrmann, P. Rajeev, T. Gupta, V. Goel, Y. Sun, A. Wiedensohler. 2022. Impact of chemical properties of human respiratory droplets and aerosol particles on airborne viruses' viability and indoor transmission. *Viruses* 14:1497. doi: 10.3390/v14071497.

Alba-Simionesco, C., B. Coasne, G. Dosseh, G. Dudziak, K. E. Gubbins, R. Radhakrishnan, M. Sliwinska-Bartkowiak. 2006. Effects of confinement on freezing and melting. *Journal of physics. Condensed matter* 18:R15. doi: 10.1088/0953-8984/18/6/R01.

Altaf, M. B. and M. A. Freedman. 2017. Effect of drying rate on aerosol particle morphology. *The Journal of Physical Chemistry Letters* 8:3613-3618. doi: 10.1021/acs.jpclett.7b01327.

Ault, A. P. and J. L. Axson. 2017. Atmospheric aerosol chemistry: Spectroscopic and microscopic advances. *Analytical Chemistry* 89:430-452. doi: 10.1021/acs.analchem.6b04670.

Baustian, K. J., D. J. Cziczo, M. E. Wise, K. A. Pratt, G. Kulkarni, A. G. Hallar, M. A. Tolbert. 2012. Importance of aerosol composition, mixing state, and morphology for heterogeneous ice nucleation: A combined field and laboratory approach. *Journal of Geophysical Research: Atmospheres* 117:n/a-n/a. doi: 10.1029/2011jd016784.

Beall, C. M., D. Lucero, T. C. Hill, P. J. Demott, M. D. Stokes, K. A. Prather. 2020. Best practices for precipitation sample storage for offline studies of ice nucleation in marine and coastal environments. *Atmospheric Measurement Techniques* 13:6473-6486. doi: 10.5194/amt-13-6473-2020.

Beall, C. M., J. M. Michaud, M. A. Fish, J. Dinasquet, G. C. Cornwell, M. D. Stokes, M. D. Burkart, T. C. Hill, P. J. Demott, K. A. Prather. 2021. Cultivable halotolerant ice-nucleating bacteria and fungi in coastal precipitation. *Atmospheric Chemistry and Physics* 21:9031-9045. doi: 10.5194/acp-21-9031-2021.

Bellouin, N., J. Quaas, E. Gryspeerdt, S. Kinne, P. Stier, D. Watson-Parris, O. Boucher, K. S. Carslaw, M. Christensen, A. L. Daniau, J. L. Dufresne, G. Feingold, S. Fiedler, P. Forster, A. Gettelman, J. M. Haywood, U. Lohmann, F. Malavelle, T. Mauritsen, D. T. Mccoy, G. Myhre, J. Mülmenstädt, D. Neubauer, A. Possner, M. Rugenstein, Y. Sato, M. Schulz, S. E. Schwartz, O. Sourdeval, T. Storelvmo, V. Toll, D. Winker, B. Stevens. 2020. Bounding global aerosol radiative forcing of climate change. *Reviews of Geophysics* 58. doi: 10.1029/2019rg000660.

Benison, K. C. 2019. How to search for life in martian chemical sediments and their fluid and solid inclusions using petrographic and spectroscopic methods. *Frontiers in Environmental Science* 7. doi.

Bertram, T. H., R. E. Cochran, V. H. Grassian, E. A. Stone. 2018. Sea spray aerosol chemical composition: Elemental and molecular mimics for laboratory studies of heterogeneous and multiphase reactions. *Chemical Society Reviews* 47:2374-2400. doi: 10.1039/c7cs00008a.

Brubaker, T., M. Polen, P. Cheng, V. Ekambaram, J. Somers, S. L. Anna, R. C. Sullivan. 2020. Development and characterization of a "store and create" microfluidic device to determine the heterogeneous freezing properties of ice nucleating particles. *Aerosol Science and Technology* 54:79-93. doi: 10.1080/02786826.2019.1679349.

Burrows, S. M., W. Elbert, M. G. Lawrence, U. Pöschl. 2009. Bacteria in the global atmosphere – part 1: Review and synthesis of literature data for different ecosystems. *Atmospheric Chemistry and Physics* 9:9263-9280. doi: 10.5194/acp-9-9263-2009.

Cesur, R. M., I. M. Ansari, F. Chen, B. C. Clark, M. A. Schneegurt. 2021. Bacterial growth in brines formed by the deliquescence of salts relevant to cold arid worlds. *Astrobiology* 22:104-115. doi: 10.1089/ast.2020.2336.

Chen, J., X. Pei, H. Wang, J. Chen, Y. Zhu, M. Tang, Z. Wu. 2018. Development, characterization, and validation of a cold stage-based ice nucleation array (pku-ina). *Atmosphere* 9:357. doi: 10.3390/atmos9090357.

Demott, P. J., D. J. Cziczo, A. J. Prenni, D. M. Murphy, S. M. Kreidenweis, D. S. Thomson, R. Borys, D. C. Rogers. 2003. Measurements of the concentration and composition of nuclei for cirrus formation. *Proceedings of the National Academy of Sciences* 100:14655-14660. doi: 10.1073/pnas.2532677100.

Demott, P. J., T. C. J. Hill, C. S. Mccluskey, K. A. Prather, D. B. Collins, R. C. Sullivan, M. J. Ruppel, R. H. Mason, V. E. Irish, T. Lee, C. Y. Hwang, T. S. Rhee, J. R. Snider, G. R. Mcmeeking, S. Dhaniyala, E. R. Lewis, J. J. B. Wentzell, J. Abbatt, C. Lee, C. M. Sultana, A. P. Ault, J. L. Axson, M. Diaz Martinez, I. Venero, G. Santos-Figueroa, M. D. Stokes, G. B. Deane, O. L. Mayol-Bracero, V. H. Grassian, T. H. Bertram, A. K. Bertram, B. F. Moffett, G. D. Franc. 2016. Sea spray aerosol as a unique source of ice nucleating particles. *Proceedings of the National Academy of Sciences* 113:5797-5803. doi: 10.1073/pnas.1514034112.

Elabed, H., E. González-Tortuero, C. Ibacache-Quiroga, A. Bakhrouf, P. Johnston, K. Gaddour, J. Blázquez, A. Rodríguez-Rojas. 2019. Seawater salt-trapped pseudomonas aeruginosa survives for years and gets primed for salinity tolerance. *BMC Microbiology* 19. doi: 10.1186/s12866-019-1499-2.

Gao, K., F. Friebel, C.-W. Zhou, Z. A. Kanji. 2022. Enhanced soot particle ice nucleation ability induced by aggregate compaction and densification. *Atmospheric Chemistry and Physics* 22:4985-5016. doi: 10.5194/acp-22-4985-2022.

Ginot, F., T. Lenavetier, D. Dedovets, S. Deville. 2020. Solute strongly impacts freezing under confinement. *Applied Physics Letters* 116:253701. doi: 10.1063/5.0008925.

Haixia, C. and C. Guoxiang. 2015. Determining fluid compositions in the h2o-nacl-cacl2system with cryogenic raman spectroscopy: Application to natural fluid inclusions. *Acta Geologica Sinica - English Edition* 89:894-901. doi: 10.1111/1755-6724.12487.

Hasenkopf, C. A., D. P. Veghte, G. P. Schill, S. Lodoysamba, M. A. Freedman, M. A. Tolbert. 2016. Ice nucleation, shape, and composition of aerosol particles in one of the most polluted cities in the world: Ulaanbaatar, mongolia. *Atmospheric Environment* 139:222-229. doi: https://doi.org/10.1016/j.atmosenv.2016.05.037.

Hawkins, L. N. and L. M. Russell. 2010. Polysaccharides, proteins, and phytoplankton fragments: Four chemically distinct types of marine primary organic aerosol classified by single particle spectromicroscopy. *Advances in Meteorology* 2010:1-14. doi: 10.1155/2010/612132.

Hidy, G. M. 2019. Atmospheric aerosols: Some highlights and highlighters, 1950 to 2018. *Aerosol Science and Engineering* 3:1-20. doi: 10.1007/s41810-019-00039-0.

Hinds, W. C. 1999. Aerosol technology : Properties, behavior, and measurement of airborne particles. doi.

Isenrich, F. N., N. Shardt, M. Rösch, J. Nette, S. Stavrakis, C. Marcolli, Z. A. Kanji, A. J. Demello, U. Lohmann. 2022. The microfluidic ice nuclei counter zürich (mincz): A platform for homogeneous and heterogeneous ice nucleation. *Atmospheric Measurement Techniques* 15:5367-5381. doi: 10.5194/amt-15-5367-2022.

Jahl, L. G., T. A. Brubaker, M. J. Polen, L. G. Jahn, K. P. Cain, B. B. Bowers, W. D. Fahy, S. Graves, R. C. Sullivan. 2021. Atmospheric aging enhances the ice nucleation ability of biomass-burning aerosol. *Science Advances* 7:eabd3440. doi: 10.1126/sciadv.abd3440.

Jayarathne, T., C. M. Sultana, C. Lee, F. Malfatti, J. L. Cox, M. A. Pendergraft, K. A. Moore, F. Azam, A. V. Tivanski, C. D. Cappa, T. H. Bertram, V. H. Grassian, K. A. Prather, E. A. Stone. 2016. Enrichment of saccharides and divalent cations in sea spray aerosol during two phytoplankton blooms. *Environmental Science & Technology* 50:11511-11520. doi: 10.1021/acs.est.6b02988.

Kaluarachchi, C. P., V. W. Or, Y. Lan, E. S. Hasenecz, D. Kim, C. K. Madawala, G. P. Dorcé, K. J. Mayer, J. S. Sauer, C. Lee, C. D. Cappa, T. H. Bertram, E. A. Stone, K. A. Prather, V. H. Grassian, A. V. Tivanski. 2022. Effects of atmospheric aging processes on nascent sea spray aerosol physicochemical properties. *ACS Earth and Space Chemistry* 6:2732-2744. doi: 10.1021/acsearthspacechem.2c00258.

Karimi, B., R. Nosrati, B. S. Fazly Bazzaz, M. Mirpour, M. Malboobi, P. Owlia. 2020. A comparative evaluation of freezing criteria and molecular characterization of epiphytic ice-nucleating (ice+) and non-ice-nucleating (ice−) pseudomonas syringae and pseudomonas fluorescens. *Journal of Plant Pathology* 102:169-178. doi: 10.1007/s42161-019-00402-7.

Keene, W. C., H. Maring, J. R. Maben, D. J. Kieber, A. A. P. Pszenny, E. E. Dahl, M. A. Izaguirre, A. J. Davis, M. S. Long, X. Zhou, L. Smoydzin, R. Sander. 2007. Chemical and physical characteristics of nascent aerosols produced by bursting bubbles at a model air-sea interface. *Journal of Geophysical Research* 112. doi: 10.1029/2007jd008464.

Knopf, D. A., P. A. Alpert, B. Wang. 2018. The role of organic aerosol in atmospheric ice nucleation: A review. *ACS Earth and Space Chemistry* 2:168-202. doi: 10.1021/acsearthspacechem.7b00120.

Kohler, F., O. Pierre-Louis, D. K. Dysthe. 2022. Crystal growth in confinement. *Nature Communications* 13. doi: 10.1038/s41467-022-34330-5.

Korolev, A., G. Mcfarquhar, P. R. Field, C. Franklin, P. Lawson, Z. Wang, E. Williams, S. J. Abel, D. Axisa, S. Borrmann, J. Crosier, J. Fugal, M. Krämer, U. Lohmann, O. Schlenczek, M. Schnaiter, M. Wendisch. 2017. Mixed-phase clouds: Progress and challenges. *Meteorological Monographs* 58:5.1-5.50. doi: 10.1175/amsmonographs-d-17-0001.1.

Krieger, U. K., C. Marcolli, J. P. Reid. 2012. Exploring the complexity of aerosol particle properties and processes using single particle techniques. *Chemical Society Reviews* 41:6631. doi: 10.1039/c2cs35082c.

Legh-Land, V., A. E. Haddrell, D. Lewis, D. Murnane, J. P. Reid. 2021. Water uptake by evaporating pmdi aerosol prior to inhalation affects both regional and total deposition in the respiratory system. *Pharmaceutics* 13:941. doi: 10.3390/pharmaceutics13070941.

Lei, Z., Y. Chen, Y. Zhang, M. E. Cooke, I. R. Ledsky, N. C. Armstrong, N. E. Olson, Z. Zhang, A. Gold, J. D. Surratt, A. P. Ault. 2022. Initial ph governs secondary organic aerosol phase state and morphology after uptake of isoprene epoxydiols (iepox). *Environmental Science & Technology* 56:10596-10607. doi: 10.1021/acs.est.2c01579.

Li, L., J. R. Sanchez, F. Kohler, A. Røyne, D. K. Dysthe. 2018. Microfluidic control of nucleation and growth of caco₃. *Crystal Growth & Design* 18:4528-4535. doi: 10.1021/acs.cgd.8b00508.

Lindsley, W. G., T. A. Pearce, J. B. Hudnall, K. A. Davis, S. M. Davis, M. A. Fisher, R. Khakoo, J. E. Palmer, K. E. Clark, I. Celik, C. C. Coffey, F. M. Blachere, D. H. Beezhold. 2012. Quantity and size distribution of cough-generated aerosol particles produced by influenza patients during and after illness. *Journal of Occupational and Environmental Hygiene* 9:443-449. doi: 10.1080/15459624.2012.684582.

Mael, L. E., H. Busse, V. H. Grassian. 2019. Measurements of immersion freezing and heterogeneous chemistry of atmospherically relevant single particles with micro-raman spectroscopy. *Analytical Chemistry* 91:11138-11145. doi: 10.1021/acs.analchem.9b01819.

Mahrt, F., C. Rösch, K. Gao, C. H. Dreimol, M. A. Zawadowicz, Z. A. Kanji. 2023. Physicochemical properties of charcoal aerosols derived from biomass pyrolysis affect their ice-nucleating abilities at cirrus and mixed-phase cloud conditions. *Atmospheric Chemistry and Physics* 23:1285-1308. doi: 10.5194/acp-23-1285-2023.

Marcolli, C. 2014. Deposition nucleation viewed as homogeneous or immersion freezing in pores and cavities. *Atmospheric Chemistry and Physics* 14:2071-2104. doi: 10.5194/acp-14-2071-2014.

Mccoy, D. T., I. Tan, D. L. Hartmann, M. D. Zelinka, T. Storelvmo. 2016. On the relationships among cloud cover, mixed-phase partitioning, and planetary albedo in gcms. *Journal of Advances in Modeling Earth Systems* 8:650-668. doi: 10.1002/2015ms000589.

Meldrum, F. C. and C. O'Shaughnessy. 2020. Crystallization in confinement. *Advanced Materials* 32:2001068. doi: 10.1002/adma.202001068.

Mukherjee, P., J. R. Reinfelder, Y. Gao. 2020. Enrichment of calcium in sea spray aerosol in the arctic summer atmosphere. *Marine Chemistry* 227:103898. doi: https://doi.org/10.1016/j.marchem.2020.103898.

Nandy, L. and C. S. Dutcher. 2018. Phase behavior of ammonium sulfate with organic acid solutions in aqueous aerosol mimics using microfluidic traps. *The Journal of Physical Chemistry B* 122:3480-3490. doi: 10.1021/acs.jpcb.7b10655.

Nandy, L., S. Liu, C. Gunsbury, X. Wang, M. A. Pendergraft, K. A. Prather, C. S. Dutcher. 2019. Multistep phase transitions in sea surface microlayer droplets and aerosol mimics using microfluidic wells. *ACS Earth and Space Chemistry* 3:1260-1267. doi: 10.1021/acsearthspacechem.9b00121.

Narayan, S., I. Makhnenko, D. B. Moravec, B. G. Hauser, A. J. Dallas, C. S. Dutcher. 2020. Insights into the microscale coalescence behavior of surfactant-stabilized droplets using a microfluidic hydrodynamic trap. *Langmuir* 36:9827-9842. doi: 10.1021/acs.langmuir.0c01414.

Narayanan, S. 2011. Gas assisted thin-film evaporation from confined spaces. *ProQuest Dissertations and Theses*:213. doi.

Oppo, C., S. Bellandi, N. Degli Innocenti, A. M. Stortini, G. Loglio, E. Schiavuta, R. Cini. 1999. Surfactant components of marine organic matter as agents for biogeochemical fractionation and pollutant transport via marine aerosols. *Marine Chemistry* 63:235-253. doi: 10.1016/s0304-4203(98)00065-6.

Ott, E.-J. E. and M. A. Freedman. 2021. Influence of ions on the size dependent morphology of aerosol particles. *ACS Earth and Space Chemistry* 5:2320-2328. doi: 10.1021/acsearthspacechem.1c00210.

Peterson, R. E. and B. J. Tyler. 2003. Surface composition of atmospheric aerosol: Individual particle characterization by tof-sims. *Applied surface science* 203:751-756. doi: 10.1016/S0169-4332(02)00812-7.

Polen, M., T. Brubaker, J. Somers, R. C. Sullivan. 2018. Cleaning up our water: Reducing interferences from nonhomogeneous freezing of "pure" water in droplet freezing assays of ice-nucleating particles. *Atmospheric Measurement Techniques* 11:5315-5334. doi: 10.5194/amt-11-5315-2018.

Polen, M., E. Lawlis, R. C. Sullivan. 2016. The unstable ice nucleation properties of snomax® bacterial particles. *Journal of Geophysical Research: Atmospheres* 121:11,666-611,678. doi: 10.1002/2016jd025251.

Reche, I., G. D'Orta, N. Mladenov, D. M. Winget, C. A. Suttle. 2018. Deposition rates of viruses and bacteria above the atmospheric boundary layer. *The ISME Journal* 12:1154-1162. doi: 10.1038/s41396-017-0042-4.

Reicher, N., C. Budke, L. Eickhoff, S. Raveh-Rubin, I. Kaplan-Ashiri, T. Koop, Y. Rudich. 2019. Size-dependent ice nucleation by airborne particles during dust events in the eastern mediterranean. *Atmospheric Chemistry and Physics* 19:11143-11158. doi: 10.5194/acp-19-11143-2019.

Reicher, N., L. Segev, Y. Rudich. 2018. The weizmann supercooled droplets observation on a microarray (wisdom) and application for ambient dust. *Atmospheric Measurement Techniques* 11:233-248. doi: 10.5194/amt-11-233-2018.

Richards, D. A.-O., K. A.-O. Trobaugh, J. A.-O. Hajek-Herrera, C. L. Price, C. S. Sheldon, J. F. Davies, R. A.-O. Davis. Ion-molecule interactions enable unexpected phase transitions in organic-inorganic aerosol. Lid - 10.1126/sciadv.Abb5643 [doi] lid - eabb5643. doi.

Riemer, N., A. P. Ault, M. West, R. L. Craig, J. H. Curtis. 2019. Aerosol mixing state: Measurements, modeling, and impacts. *Reviews of Geophysics* 57:187-249. doi: 10.1029/2018rg000615.

Roy, P., M. L. House, C. S. Dutcher. 2021. A microfluidic device for automated high throughput detection of ice nucleation of snomax®. *Micromachines* 12:296. doi: 10.3390/mi12030296.

Roy, P., S. Liu, C. S. Dutcher. 2021. Droplet interfacial tensions and phase transitions measured in microfluidic channels. *Annual Review of Physical Chemistry* 72:73-97. doi: 10.1146/annurev-physchem-090419-105522.

Roy, P., L. E. Mael, T. C. J. Hill, L. Mehndiratta, G. Peiker, M. L. House, P. J. Demott, V. H. Grassian, C. S. Dutcher. 2021. Ice nucleating activity and residual particle morphology of bulk seawater and sea surface microlayer. *ACS Earth and Space Chemistry* 5:1916-1928. doi: 10.1021/acsearthspacechem.1c00175.

Roy, P., L. E. Mael, I. Makhnenko, R. Martz, V. H. Grassian, C. S. Dutcher. 2020. Temperature-dependent phase transitions of aqueous aerosol droplet systems in microfluidic traps. *ACS Earth and Space Chemistry* 4:1527-1539. doi: 10.1021/acsearthspacechem.0c00114.

Salter, M. E., E. Hamacher-Barth, C. Leck, J. Werner, C. M. Johnson, I. Riipinen, E. D. Nilsson, P. Zieger. 2016. Calcium enrichment in sea spray aerosol particles. *Geophysical Research Letters* 43:8277-8285. doi: 10.1002/2016gl070275.

Schill, S., S. Burrows, E. Hasenecz, E. Stone, T. Bertram. 2018. The impact of divalent cations on the enrichment of soluble saccharides in primary sea spray aerosol. *Atmosphere* 9:476. doi: 10.3390/atmos9120476.

Schwidetzky, R., A. T. Kunert, M. Bonn, U. Pöschl, H. Ramløv, A. L. Devries, J. Fröhlich-Nowoisky, K. Meister. 2020. Inhibition of bacterial ice nucleators is not an intrinsic property of antifreeze proteins. *The Journal of Physical Chemistry B* 124:4889-4895. doi: 10.1021/acs.jpcb.0c03001.

Sievering, H. 2004. Aerosol non-sea-salt sulfate in the remote marine boundary layer under clear-sky and normal cloudiness conditions: Ocean-derived biogenic alkalinity enhances sea-salt sulfate production by ozone oxidation. *Journal of Geophysical Research* 109. doi: 10.1029/2003jd004315.

Silva, D. A., A. C. F. Brito, R. C. M. De Paula, J. P. A. Feitosa, H. C. B. Paula. 2003. Effect of mono and divalent salts on gelation of native, na and deacetylated sterculia striata and sterculia urens polysaccharide gels. *Carbohydrate Polymers* 54:229-236. doi: 10.1016/s0144-8617(03)00163-2.

Stan, C. A., G. F. Schneider, S. S. Shevkoplyas, M. Hashimoto, M. Ibanescu, B. J. Wiley, G. M. Whitesides. 2009. A microfluidic apparatus for the study of ice nucleation in supercooled water drops. *Lab on a Chip* 9:2293. doi: 10.1039/b906198c.

Steiner, A. L., S. D. Brooks, C. Deng, D. C. O. Thornton, M. W. Pendleton, V. Bryant. 2015. Pollen as atmospheric cloud condensation nuclei. *Geophysical Research Letters* 42:3596-3602. doi: 10.1002/2015gl064060.

Stevens, R. and A. Dastoor. 2019. A review of the representation of aerosol mixing state in atmospheric models. *Atmosphere* 10:168. doi: 10.3390/atmos10040168.

Suski, K. J., T. C. J. Hill, E. J. T. Levin, A. Miller, P. J. Demott, S. M. Kreidenweis. 2018. Agricultural harvesting emissions of ice-nucleating particles. *Atmospheric Chemistry and Physics* 18:13755-13771. doi: 10.5194/acp-18-13755-2018.

Szopa, S., V. Naik, B. Adhikary, P. Artaxo, T. Berntsen, W. D. Collins, S. Fuzzi, L. Gallardo, A. Kiendler-Scharr, Z. Klimont, H. Liao, N. Unger, P. Zanis. 2021. Short-lived climate forcers, in *Climate Change 2021: The Physical Science Basis. Contribution of Working Group I to the Sixth Assessment Report of the Intergovernmental Panel on Climate Change* 817–922. Cambridge University Press, Cambridge, United Kingdom and New York, NY, USA.

Tarn, M. D., S. N. F. Sikora, G. C. E. Porter, J.-U. Shim, B. J. Murray. 2021. Homogeneous freezing of water using microfluidics. *Micromachines* 12:223. doi: 10.3390/mi12020223.

Turner, M. A., F. Arellano, L. M. Kozloff. 1990. Three separate classes of bacterial ice nucleation structures. *Journal of Bacteriology* 172:2521-2526. doi: 10.1128/jb.172.5.2521-2526.1990.

Vali, G. 1971. Quantitative evaluation of experimental results an the heterogeneous freezing nucleation of supercooled liquids. *Journal of the Atmospheric Sciences* 28:402-409. doi: 10.1175/1520-0469(1971)028<0402:qeoera>2.0.co;2.

Vazquez De Vasquez, M. G., B. A. Wellen Rudd, M. D. Baer, E. E. Beasley, H. C. Allen. 2021. Role of hydration in magnesium versus calcium ion pairing with carboxylate: Solution and the aqueous interface. *The Journal of Physical Chemistry B* 125:11308-11319. doi: 10.1021/acs.jpcb.1c06108.

Vergara-Temprado, J., A. K. Miltenberger, K. Furtado, D. P. Grosvenor, B. J. Shipway, A. A. Hill, J. M. Wilkinson, P. R. Field, B. J. Murray, K. S. Carslaw. 2018. Strong control of southern ocean cloud reflectivity by ice-nucleating particles. *Proceedings of the National Academy of Sciences* 115:2687-2692. doi: 10.1073/pnas.1721627115.

Vu, D., S. Gao, T. Berte, M. Kacarab, Q. Yao, K. Vafai, A. Asa-Awuku. 2019. External and internal cloud condensation nuclei (ccn) mixtures: Controlled laboratory studies of varying mixing states. *Atmospheric Measurement Techniques* 12:4277-4289. doi: 10.5194/amt-12-4277-2019.

Vuong, S. M. and S. L. Anna. 2012. Tuning bubbly structures in microchannels. *Biomicrofluidics* 6:022004. doi: 10.1063/1.3693605.

Wang, Z., M. Ordoubadi, H. Wang, R. Vehring. 2021. Morphology and formation of crystalline leucine microparticles from a co-solvent system using multi-orifice monodisperse spray drying. *Aerosol Science and Technology* 55:901-919. doi: 10.1080/02786826.2021.1904129.

Wex, H., S. Augustin-Bauditz, Y. Boose, C. Budke, J. Curtius, K. Diehl, A. Dreyer, F. Frank, S. Hartmann, N. Hiranuma, E. Jantsch, Z. A. Kanji, A. Kiselev, T. Koop, O. Möhler, D. Niedermeier, B. Nillius, M. Rösch, D. Rose, C. Schmidt, I. Steinke, F. Stratmann. 2015. Intercomparing different devices for the investigation of ice nucleating particles using snomax® as test substance. *Atmospheric Chemistry and Physics* 15:1463-1485. doi: 10.5194/acp-15-1463-2015.

Yao, Y., J. H. Curtis, J. Ching, Z. Zheng, N. Riemer. 2022. Quantifying the effects of mixing state on aerosol optical properties. *Atmospheric Chemistry and Physics* 22:9265-9282. doi: 10.5194/acp-22-9265-2022.

Zhang, C., Y. Zhang, M. J. Wolf, L. Nichman, C. Shen, T. B. Onasch, L. Chen, D. J. Cziczo. 2020. The effects of morphology, mobility size, and secondary organic aerosol (soa) material coating on the ice nucleation activity of black carbon in the cirrus regime. *Atmospheric Chemistry and Physics* 20:13957-13984. doi: 10.5194/acp-20-13957-2020.

Captions

Figure 1. Schematic of the microfluidic device showing a) the view of all wells as well as the inlet and outlet channels, and b) detail of one well with relevant dimensions.

Figure 2. a) Simplified schematic of large well array device showing thermocouple channels (not to scale). b) Similar design by Brubaker et al. 2020 for a 720 well device. (Brubaker et al. 2020)

Figure 3. Ice nucleating active site density, or $\eta_{m,}$ for our microfluidic device compared to several sets of literature values (Wex et al. 2015), (Polen, Lawlis and Sullivan 2016), (Brubaker et al. 2020),(Roy, House and Dutcher 2021). Horizontal error bars represent uncertainty in the temperature measurement of our device.

Figure 4. a) Frozen fraction versus temperature and b) INAS versus temperature for 1 M NaCl and 0.03mg/mL Snomax (red circles), 5.25:1 Mix and 0.03mg/mL Snomax (purple squares), and 1M $CaCl_2$ and 0.03mg/mL Snomax (blue triangles) with heat treatments applied. Crosses on plot a) indicate the background freezing curve of pure water for these samples.

Figure 5. Example images of each particle category. The categories are as follows: Single crystals a) with aggregate and b) without aggregate, c) fractal, d) and e) fully aggregate clusters, and f) amorphous.

Figure 6. Charts showing the fraction of each particle type for a) 1 M NaCl and b) 5.25:1 Mix. The ± 4% error bars represent the average deviation in value between two different devices containing the same mixture. Crosshatches in single category in b) represent aggregate surrounding the single particle, which was found in all single particles in the 5.25:1 Mix.

Figure 7. The particle distributions and their mean and median freezing temperatures for a) 1 M NaCl, b) 1M NaCl, 0.03 mg/mL Snomax, c) 1M NaCl, 0.03 mg/mL Snomax heat treated for 7 minutes, and d) 1M NaCl, 0.03 mg/mL Snomax heat treated for 10 minutes.

	Snomax (mg/mL)	**NaCl (M)**	**$CaCl_2$ (M)**
Pure NaCl	0	1	0
Pure $CaCl_2$	0	0	1
Pure 5.25:1 Mix	0	0.84	0.16
NaCl+SM	0.03	1	0
$CaCl_2$+SM	0.03	0	1
5.25:1 Mix +SM	0.03	0.84	0.16

Table 1: Ingredients of each mixture.

Supplemental Information for

Microfluidic platform for coupled studies of freezing behavior and final effloresced particle morphology in Snomax® containing aqueous droplets

Margaret L. House[a], Cari S. Dutcher[a],[b]

[a] Chemical Engineering, University of Minnesota Twin Cities, Minneapolis , MN, USA; [b] Mechanical Engineering, University of Minnesota Twin Cities, Minneapolis , MN, USA

Contents

1 Calibration And Temperature Error

1.1 Thermocouple Variance

Four thermocouples were placed in the device to measure temperature, one in each corner of the device. The variance between the four thermocouple temperatures were highly dependent upon the location of the airflow above the device. A high flow rate of dry nitrogen gas is required to prevent condensation, but if the airstream was close to a thermocouple, the measured temperature would change. When airflow was properly balanced, the variance between all thermocouples was approximately 2°C. Temperature of the device was measured as the average of the four thermocouples.

1.2 Calibration Method and Curve

Like other microfluidic freezing devices of this type, calibration was done using the standard melting temperature of hydrocarbons. For our devices, we chose the melting point of water and the melting point of dodecyne. We planned to also include the melting temperatures of decane and dodcecane, but found that these hydrocarbons dissolved the PDMS device and led to debonding during testing. The final calibration curve is shown in Figure S1, with the x-axis representing the measured temperature read raw from the actual, corrected temperature obtained by comparing with literature values of the melting point. Warming rates of 0.5°C per minute were used to ensure that the process was steady-state. Due to temperature gradients across the device, the melting point for dodecyne did not occur at one temperature. Rather, the midpoint temperature, when 50% of the wells were melted, was used. It was found that when held at this midpoint temperature, the rest of the wells would melt.

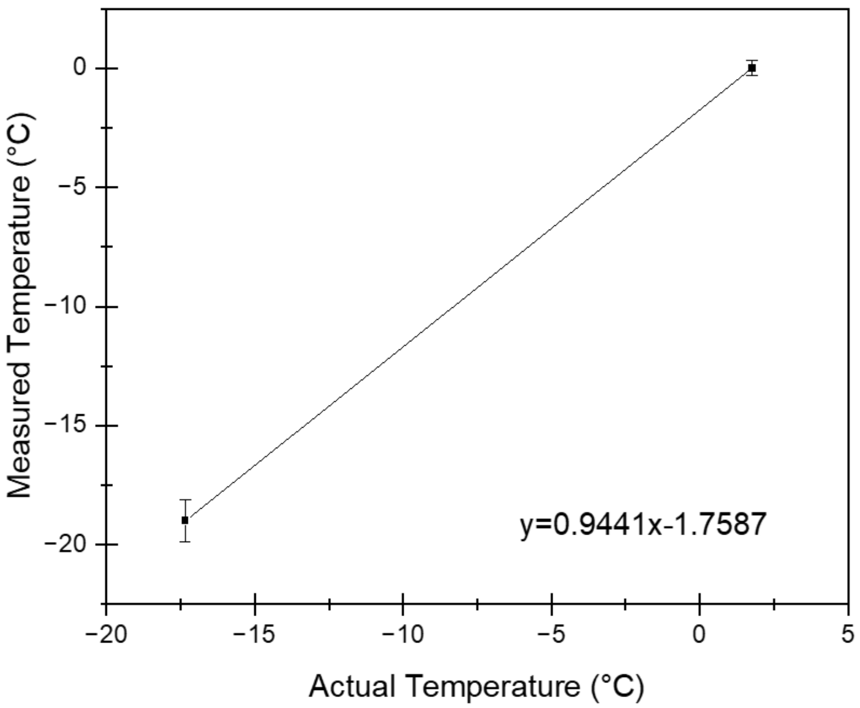

Figure S1: The thermocouple calibration curve generated from melting point measurements of water and dodecyne.

1.3 Error Bars for Temperature

Error bars for temperature measurements were calculated from standard deviation of the melting point of water and dodecyne over three tests for each substance. The error value for temperature measurements between the melting point of water and dodecyne and below the melting point of dodecyne were calculated via linear interpolation/extrapolation. The deviation from test to test was higher at lower temperatures, due to the fact that a higher dry nitrogen gas flow rate was required to prevent condensation at lower temperatures. The convection introduced in the chamber due to the gas flow rate led to thermocouple measurement instability. Error bars for the distribution of particle morphologies were calculated by using the average variation between 3 to 5 devices containing the same mixture, dried at the same rate.

2 Photolithography Techniques and Device Fabrication

2.1 Photolithography Techniques

In brief, a 4” silicon wafer (University Wafer, South Boston, MA, USA) was cleaned in “piranha solution”, a mixture of sulfuric acid and hydrogen peroxide heated to 120°C. The wafer was then thoroughly dried before a sheet of 150 μm SUEX Thick Dry Film Sheets (DJ MicroLaminates, Inc. Sudbury, MA, USA) was affixed to the wafer surface. This sheet of solvent-developed negative photoresist polymer ensures an even channel thickness across the device. A negative vinyl mask is affixed to the wafer and exposed to UV light for the manufacturer recommended duration . Finally, the photoresist is developed in PGMEA (propylene glycol methyl ether acetate), leaving behind only the mask pattern to be used as a mold. The mold is treated with silane before use to prevent devices from sticking to it.

2.2 Device Fabrication

To make microfluidic devices, polydimethylsiloxane (PDMS) polymer (Sylgard 184, Dow) is poured over the patterned mold and then degassed in a vacuum chamber and cured for 24 hours at 70°C. Glass slides are spin coated with PDMS at 3000 RPM for 30 seconds and are cured for 24 hours at 70°C. Devices are peeled from the mold and holes are punched in them using a Militex 1.2mm biopsy punch. Thermocouple channels are cut into the sides of the device as shown in Figure 2a. The device is sealed to a coated glass slide using plasma treatment (Harrick Plasma). After a post-sealing bake for 24 hours at 70° C, the devices are injected with silicone oil (Sigma Aldrich) to fill all channels and left to soak in silicone oil for a minimum of five days to ensure that they are sufficiently hydrophobic.

3 Derivative form of Ice Nucleating Active Site Density

The common equation used to calculate reported values of INAS density for Snomax-containing droplets is that of the cumulative INAS density, shown in Equation S1 (Vali 1971).

$$K(T) = -\frac{\ln\left(1 - f(T)\right)}{V \times C_m} \qquad \text{(S1)}$$

Where K(T) is the cumulative ice nucleating active site density (INAS/mg) at temperature T, V is droplet volume, f(T) is the frozen fraction at temperature T, and C_m is the bulk concentration of the ice nucleator, in this case Snomax. However, in systems with high droplet statistics spanning a broad range of freezing temperatures, the derivative INAS density, k(T), can be useful for distinguishing one type of INP from another (Vali 2019). This is calculated using Equation S2,

$$k(T) = -\frac{\ln\left(1 - \frac{\Delta N}{N(T)}\right)}{V \times C_m \times \Delta T} \qquad \text{(S2)}$$

Where k(T) is the derivative ice nucleating active site density (ΔINAS/mg*ΔT) at temperature T, ΔN is the change in the number of frozen droplets over the temperature range ΔT, N(T) is the total number of unfrozen droplets at temperature T, and V and C_m are defined in equation 1. Subtleties in IN activity

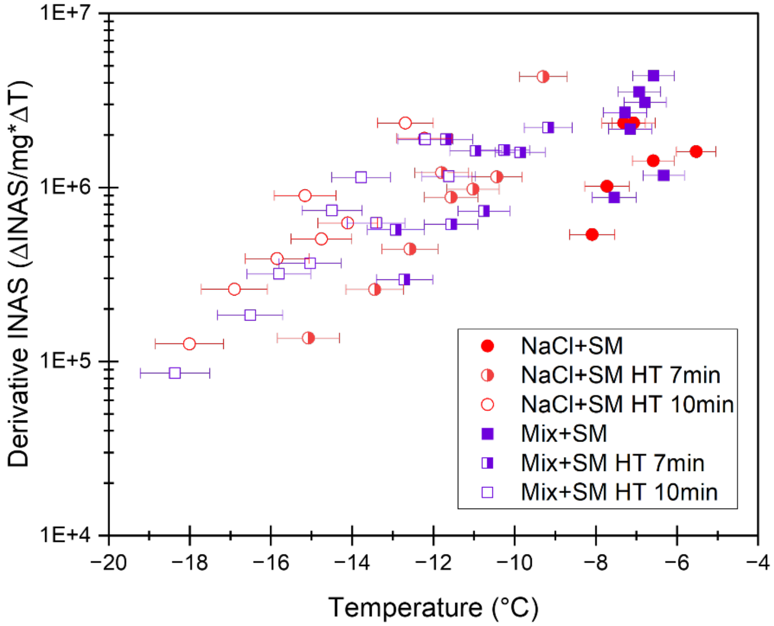

Figure S2: Derivative INAS, k(T), vs temperature for 1 M NaCl and 0.03mg/mL Snomax (red circles) and 5.25:1 Mix and 0.03mg/mL Snomax (purple squares) with heat treatments applied. All curves corrected for freezing point depression.

between the fully monovalent "NaCl+SM" case and the monovalent-divalent "Mix + SM" were of interest in our study, so we calculated the derivative INAS for these cases untreated and heat treated. The results are shown in Figure S2.

For our specific system, derivative k(T) does not elucidate any further differences between the fully monovalent case and the monovalent-divalent case. However, it is important to note that the derivative form allows for correcting of background noise and for calculating confidence limits specific to each temperature used, and is useful in many applications.

4 Refreezing Experiment

To explore the halotolerance of Snomax bacteria, fully effloresced Snomax-NaCl particles were rehydrated in a 100% humidity environment. The particles deliquesced, but never reached their initial volume (at least not in the timescale of the experiment). This led to very high salinity in the wells, to the point of supersaturation, which makes it impossible to calculate freezing point depression, which would be needed to directly compare the IN spectrum before drying and after reuptake of water. Importantly, early-freezing droplets before the efflorescence – deliquescence cycle did not match the early freezers after this cycle, suggesting some change to the IN activity of the bacteria. Figure S3 shows the relationship between freezing order in the first test, before drying, and freezing order in the second test, after drying and then deliquescence and partial rehydration.

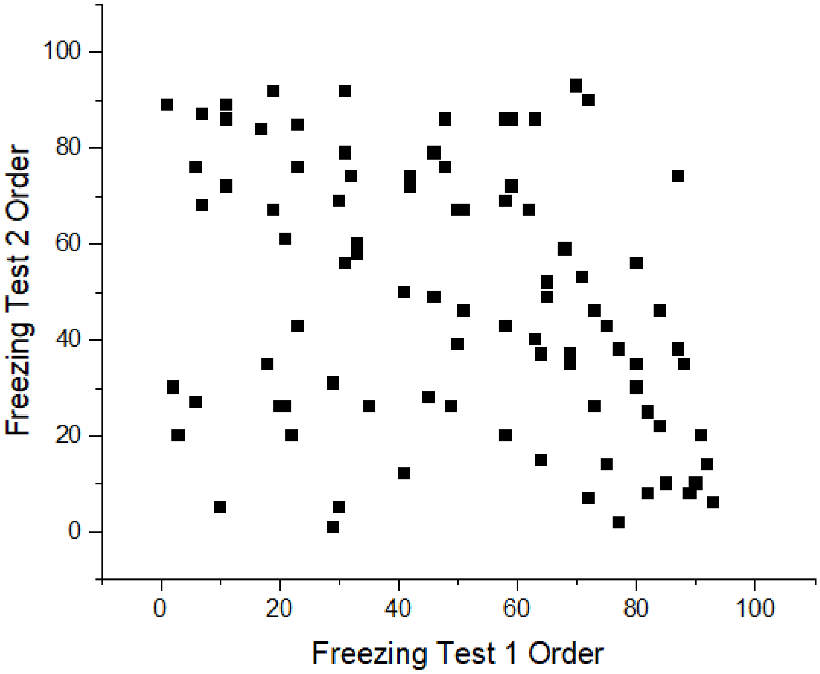

Figure S3: The freezing order of wells in Test 1 (before dehydration) and Test 2 (after a dehydration-rehydration cycle, where exposure to a high salinity environment occurred) for untreated mixture with initial concentration of 1M NaCl and 0.03 mg/mL Snomax.

Vali, G. 1971. Quantitative evaluation of experimental results an the heterogeneous freezing nucleation of supercooled liquids. *Journal of the Atmospheric Sciences* 28:402-409. doi: 10.1175/1520-0469(1971)028<0402:qeoera>2.0.co;2.

Vali, G. 2019. Revisiting the differential freezing nucleus spectra derived from drop-freezing experiments: Methods of calculation, applications, and confidence limits. *Atmospheric Measurement Techniques* 12:1219-1231. doi: 10.5194/amt-12-1219-2019.

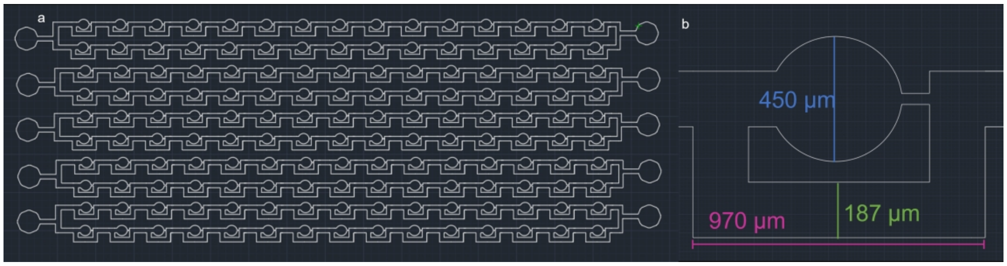

Figure 1

703x182mm (130 x 130 DPI)

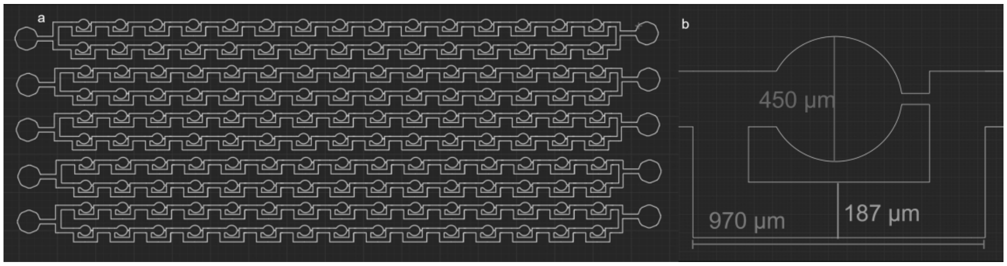

Figure 1 (grayscale version)

703x182mm (130 x 130 DPI)

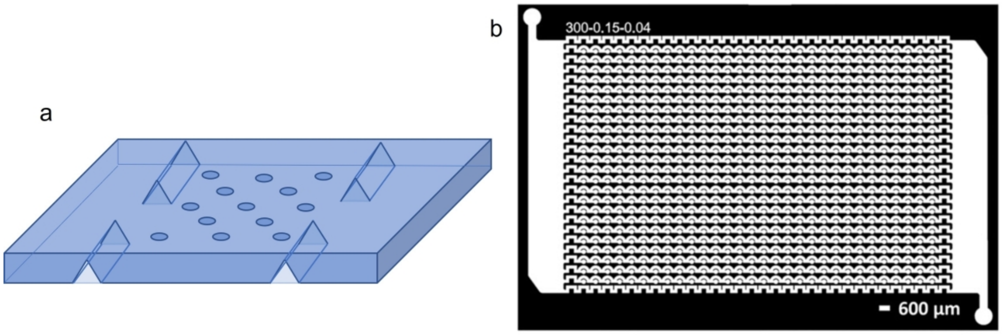

Figure 2

268x91mm (300 x 300 DPI)

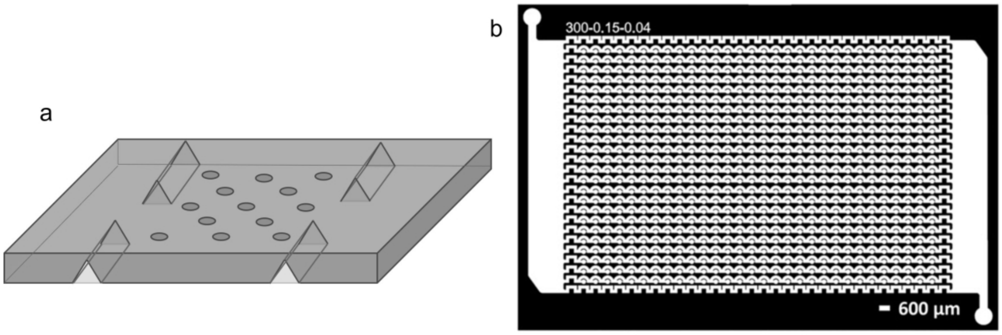

Figure 2 (grayscale version)

268x91mm (300 x 300 DPI)

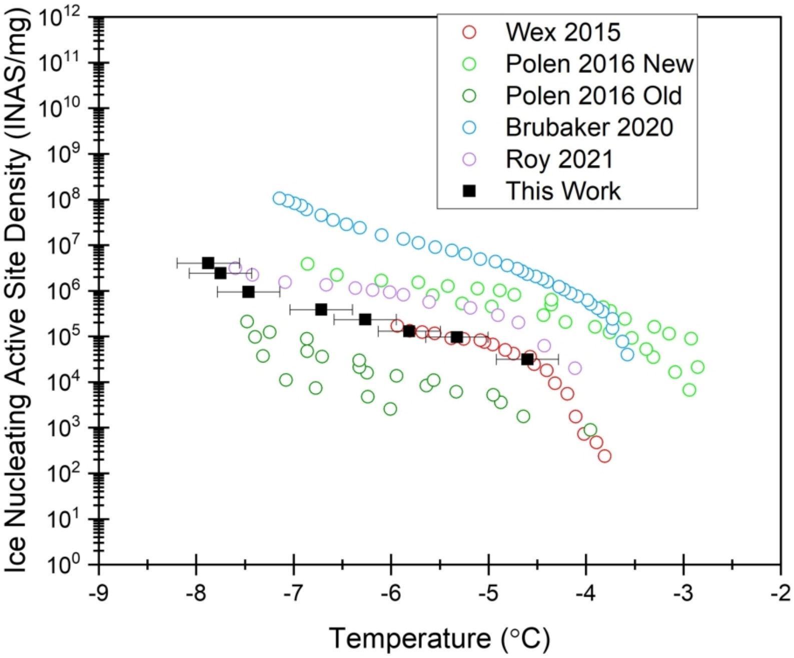

Figure 3

248x190mm (300 x 300 DPI)

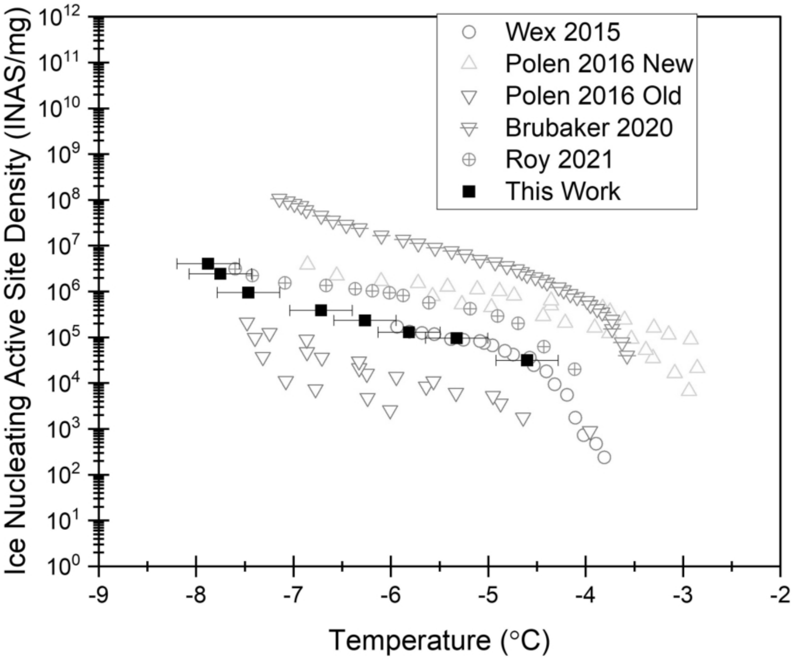

Figure 3 (grayscale version)

248x190mm (300 x 300 DPI)

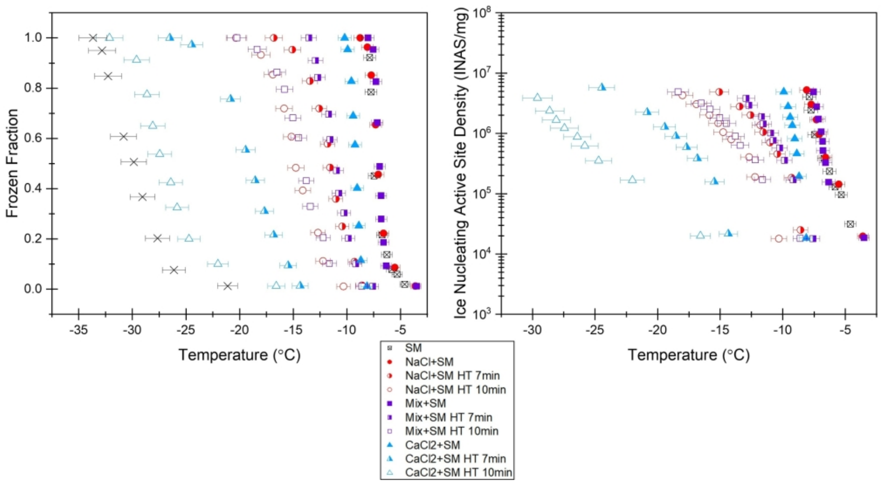

Figure 4

299x154mm (300 x 300 DPI)

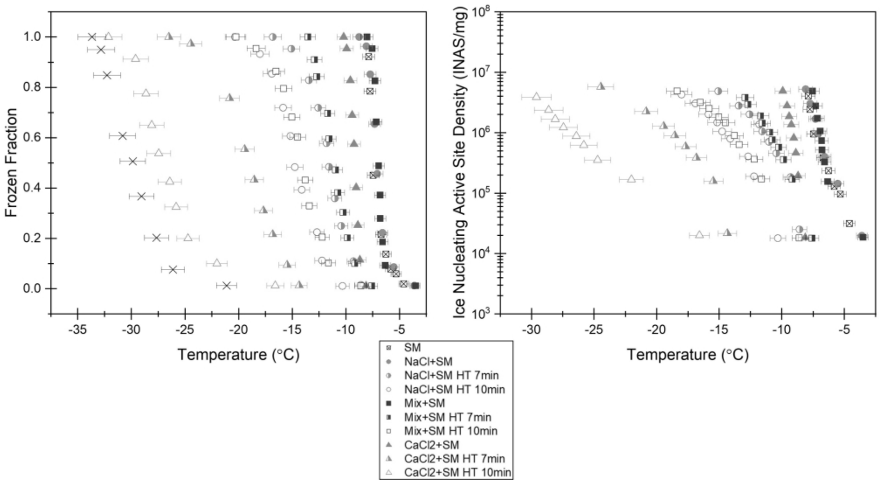

Figure 4 (grayscale version)

299x154mm (300 x 300 DPI)

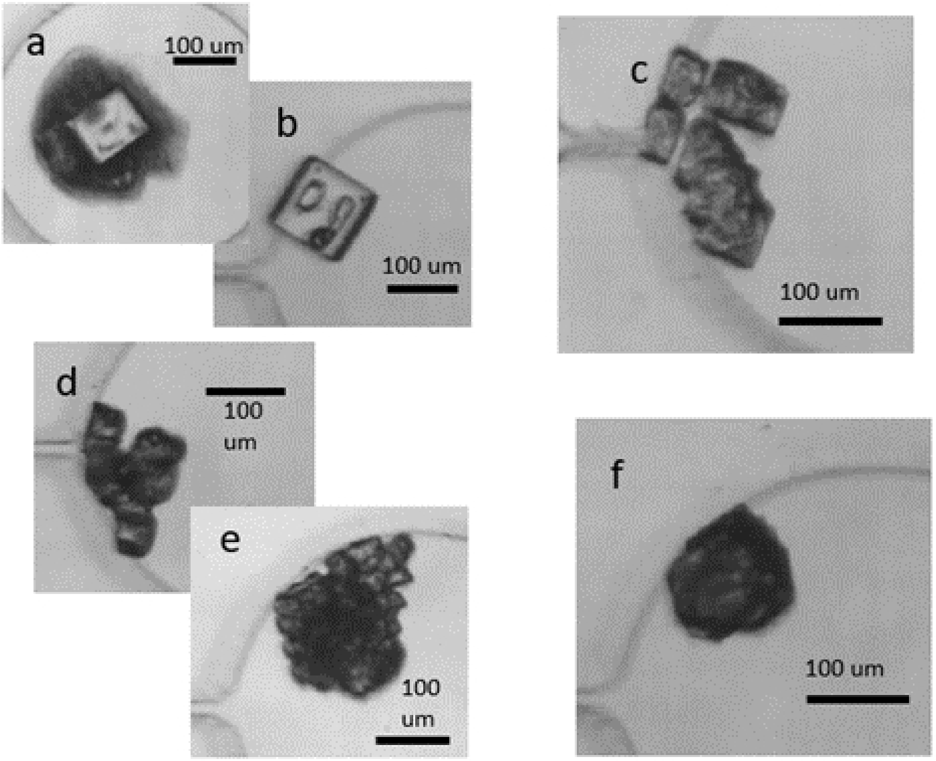

Figure 5 (both main text and grayscale)

336x280mm (38 x 38 DPI)

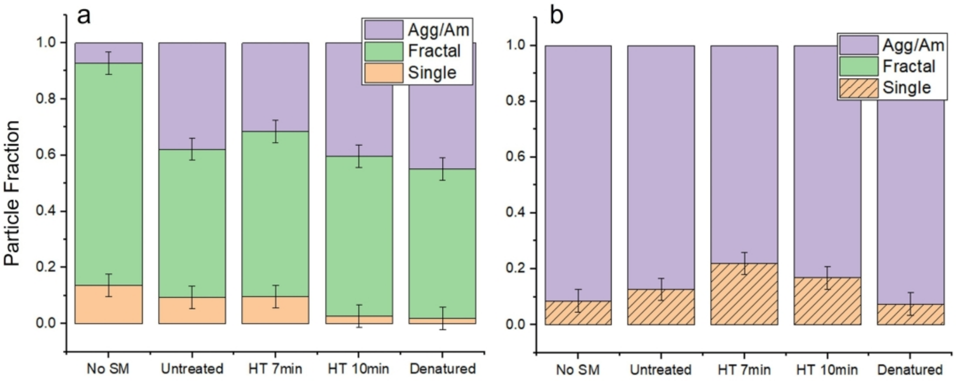

Figure 6

242x100mm (300 x 300 DPI)

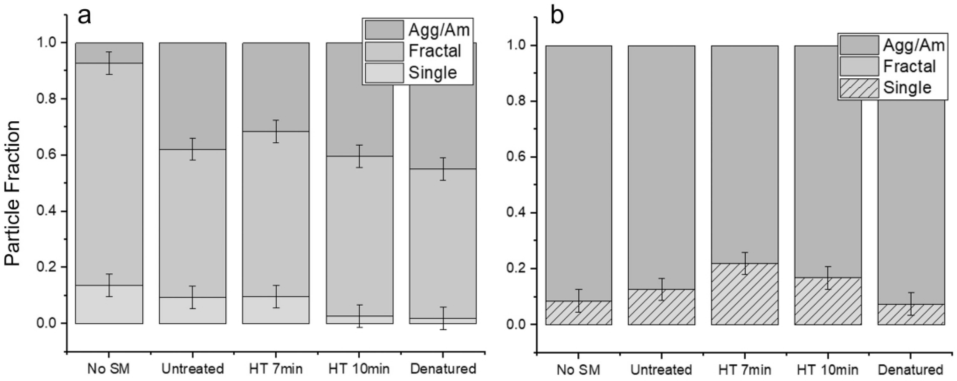

Figure 6 (grayscale version)

242x100mm (300 x 300 DPI)

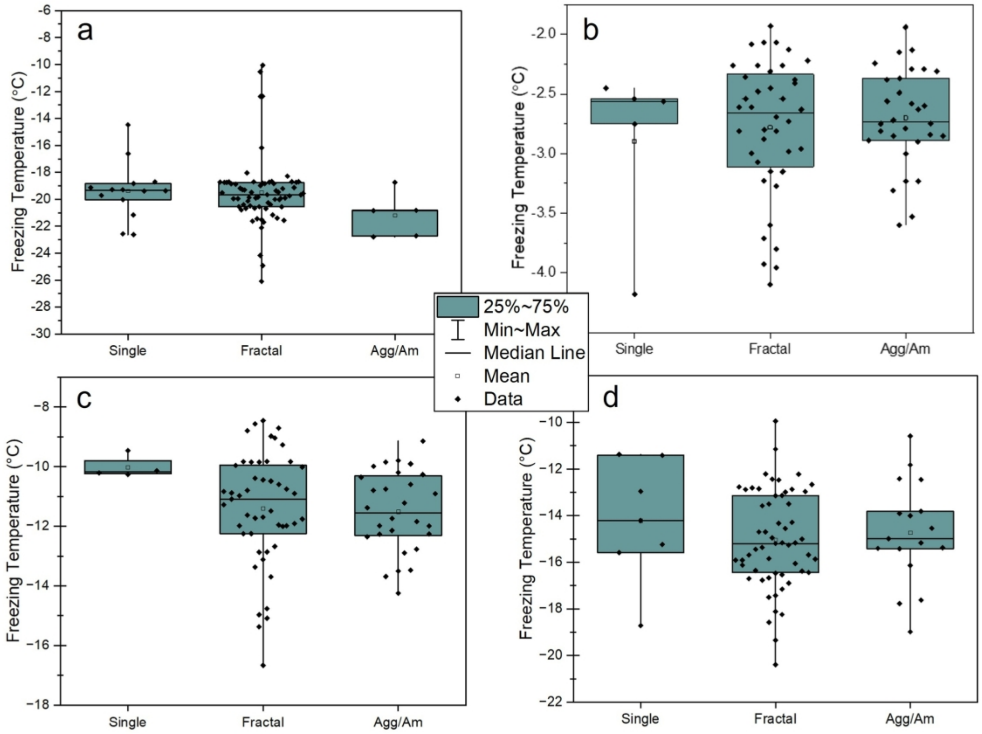

Figure 7

210x162mm (300 x 300 DPI)

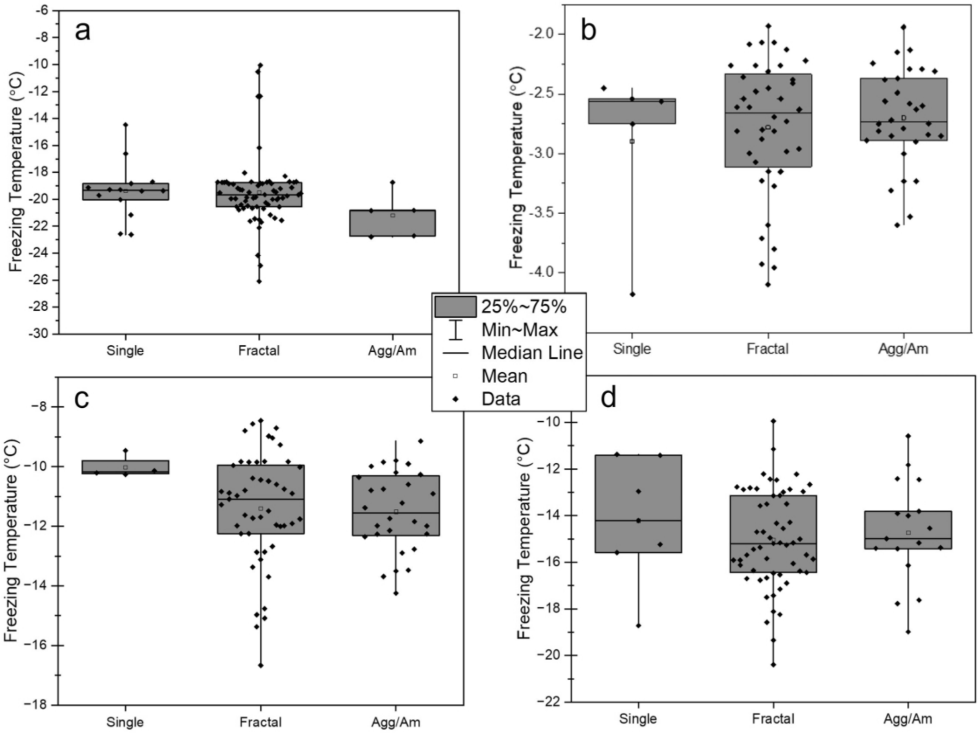

Figure 7 (grayscale version)

210x162mm (300 x 300 DPI)